ADVANCED FUNCTIONAL MATERIALS
www.afm-journal.de

Overcoming the Stability Issue for Hydrophobic Hole Transporting Layers Utilized in Tin-Lead Perovskite and Tandem Solar Cells

Chun-Hsiao Kuan, Xianyuan Jiang, Qilin Zhou, Xin Wen, Sung-Fu Hung, Hsin-Lung Chen, Yun-Sheng Shih, Sudhakar Narra, Mingyu Ma, Jau-Wern Chiou, Jhih-Min Lin, Yi Hou, and Eric Wei-Guang Diau**

The stability of all-perovskite tandem solar cells is an important issue due to the acidic nature of the hole transport layer (HTL) utilized, poly(3,4-ethylenedioxythiophene) polystyrene sulfonate (PEDOT:PSS) in tin-lead perovskite. Incorporating hydrophobic HTL, such as poly[bis(4-phenyl)(2,4,6-trimethylphenyl)amine] (PTAA), for tin-lead perovskite solar cells (TLPSCs) is often hindered by poor film coverage of the perovskite layer. Herein, a non-annealing approach is introduced to fabricate high-quality PTAA films, which enables the formation of a dense and uniform perovskite layer. It is found that SnF_2 incorporated into the perovskite precursor promotes the horizontal spreading of PTAA, facilitates the formation of dangling bonds between N and Sn, and enhances π–π interactions combined with SnF_2-induced crosslinking. Utilizing this approach in TLPSC, a record power conversion efficiency (PCE) of 22.67% is achieved for PTAA-based devices. Furthermore, when applying TLPSC to all perovskite tandem solar cells, the polymeric PTAA HTL enables a fully covered intermediate recombination layer, ultimately for the tandem device to achieve an efficiency of 28.14% with excellent operating stability, attaining 96% for 500 h at the maximum power point under simulated one-sun illumination. This study highlights the low cost, universality, and environment-friendly way of the non-annealing approach and underscores significant improvements for PTAA-based all-perovskite tandem solar cells.

1. Introduction

All-perovskite tandem solar cells represent a notable progression in photovoltaic technology,[1,2] possessing the potential to surpass the Shockley–Queisser efficiency barrier by integrating wide-bandgap lead-based perovskites with narrow-bandgap tin-lead perovskites.[3–5] Metal halide perovskites are characterized by their tunable band gaps, economical solution processing, and swiftly improving device performance, establishing them as frontrunners in next-generation solar cell applications.[6–8] Double-junction all-perovskite tandems have achieved certified efficiencies beyond 28% through buried-interface engineering and wide-narrow bandgap matching.[9] Triple-junction and quad-junction all-perovskite tandem solar cells have also been reported.[10–14] These devices employ complementary absorption characteristics to attain efficiencies near 30%.[15–17] However, stability is the paramount concern in all perovskite tandem solar cells.[18–20]

C.-H. Kuan, S.-F. Hung, Y.-S. Shih, S. Narra, E. W.-G. Diau
Department of Applied Chemistry and Institute of Molecular Science
National Yang Ming Chiao Tung University
1001 Ta-Hseuh Rd., Hsinchu 300093, Taiwan
E-mail: diau@nycu.edu.tw

C.-H. Kuan, S.-F. Hung, S. Narra, E. W.-G. Diau
Center for Emergent Functional Matter Science
National Yang Ming Chiao Tung University
1001 Ta-Hseuh Rd., Hsinchu 300093, Taiwan

The ORCID identification number(s) for the author(s) of this article can be found under https://doi.org/10.1002/adfm.202522134

DOI: 10.1002/adfm.202522134

X. Jiang, X. Wen, M. Ma
School of Physical Science and Technology
ShanghaiTech University
393 Middle Huaxia Road, Pudong New Area, Shanghai 201210, China

Q. Zhou, Y. Hou
Department of Chemical and Biomolecular Engineering
National University of Singapore
4 Engineering Drive 4, E5 #02-09, Singapore 117585, Singapore
E-mail: yi.hou@nus.edu.sg

Q. Zhou, Y. Hou
Solar Energy Research Institute of Singapore
National University of Singapore
21 Lower Kent Ridge Road, Singapore 119077, Singapore

H.-L. Chen
Department of Chemical Engineering
National Tsing Hua University
No. 101, Section 2, Kuang-Fu Road, Hsinchu 30013, Taiwan

One crucial factor in the stability of tandem solar cells is the hole transport layer (HTL). Widely employed HTLs, such as poly(3,4-ethylenedioxythiophene)-poly(styrenesulfonate) (PEDOT:PSS), exhibit hygroscopic and acidic characteristics that result in degradation and poor long-term stability of the device.[21–23] In contrast, poly[bis(4-phenyl)(2,4,6-trimethylphenyl)amine] (PTAA) combines excellent hydrophobicity with outstanding chemical and thermal robustness, making it a highly promising candidate for durable hole-transport layers.[24] However, PTAA's intrinsically low surface energy impedes uniform wetting by perovskite precursors, leading to incomplete film coverage, void formation, and reduced photovoltaic performance. Traditional wetting-enhancement strategies—such as DMF pre-treatment, PEAI-based surface modifiers or BCP+PbI_2 chelation—can restore wettability,[25,26] but they also introduce additional cost and processing complexity in the fabrication of both lead-based and tin–lead tandem perovskite solar cells.

We developed a low-cost, non-annealing method for HTLs that enables direct deposition of perovskite precursors onto unannealed HTLs. Applicable to PTAA, 2,2′,7,7′-Tetrakis-(*N*,*N*-di-4-methoxyphenylamino)-9,9′-spirobifluorene (Spiro), Di-[4-(*N*,*N*-di-p-tolyl-amino)-phenyl]cyclohexane (TAPC), and 4,4′,4″-Tris[phenyl(m-tolyl)amino]triphenylamine (m-MTDATA), this method consistently yields smooth, pin-hole-free perovskite films. This method prominently features tin fluoride (SnF_2), which functions both as a reducing agent and as a structural/electronic modifier. The non-annealing process involves the incorporation of chlorobenzene (CB), which modifies the solubility of SnF_2, facilitating its aggregation with HTL materials. SnF_2-HTL aggregates serve as nucleation cores, promoting the growth of high-quality perovskite films. SnF_2 diffuses to the HTL/perovskite interface, altering the wet HTL and improving its wettability.[27] Advanced characterization techniques, such as Small-Angle X-ray Scattering (SAXS) and X-ray Absorption Spectroscopy (XAS), demonstrate that SnF_2 enhances the polymer network structure, resulting in denser and more stable HTL-perovskite interfaces.

The performance of the device underscores the universality and robustness of the non-annealing method. PTAA-based solar cells demonstrate a PCE of 22.67%, while other HTLs attained PCE exceeding 20%, demonstrating their broad applicability. Furthermore, tandem solar cells employing non-annealing PTAA achieve a record power conversion efficiency of 28.14%, with an open-circuit voltage exceeding 2.13 V. Spiro, TAPC, and m-MTDATA-based tandem cells exhibit notable enhancements, reaching efficiencies of ≈20%. Stability testing of encapsulated tandem devices under maximum power point tracking demonstrates that they maintained 96% of their initial power conversion efficiency after prolonged exposure to simulated sunlight for 500 h, markedly exceeding the performance of conventional PEDOT:PSS-based counterparts using the annealing method.

2. Results and Discussion

The poor wettability of PTAA and other aromatic hydrocarbon-based hole transport layer materials is a major obstacle to their application in perovskite solar cells. To address this issue, we propose a non-annealing preparation method (**Figure 1a**). For convenience in naming, we add an "A" to the end of the annealed HTL, such as PTAA-A, while the unannealed HTL retains its original name, such as PTAA. The traditional HTL fabrication process requires annealing after spin-coating. However, during annealing, aromatic hydrocarbon-based HTL molecules with multiple benzene rings tend to aggregate longitudinally, forming large hydrophobic particles. The roughness of the annealed HTL is higher than that of the non-annealed HTL (Figure S1, Supporting Information).

After spin-coating the HTL, we skip the annealing step and directly drop-cast the perovskite precursor solution (Figure 1a). On the non-annealed HTL substrate, the perovskite exhibits excellent wettability (Figure S2, Supporting Information), whereas on the annealed HTL substrate, the wettability is significantly reduced. As a result, a fully covered perovskite thin film can be obtained on the non-annealed HTL substrate. In contrast, the perovskite film on the annealed HTL substrate fails to achieve complete coverage (Figure 1a; Figure S3, Supporting Information). We tested the quality of perovskite on both annealed and non-annealed HTLs. X-ray diffraction (XRD) results indicate that no significant difference in crystallinity (Figure S4, Supporting Information), and no non-perovskite phases were observed. In our case, the similar peak positions, intensities, and full width at half maximum (FWHM) in the XRD spectra, as shown in Table S1 (Supporting Information), indicate that both annealed and unannealed PTAA substrates yield perovskite films with comparable average grain size and bulk crystallinity. To further investigate this, we conducted grazing-incidence wide-angle X-ray scattering (GIWAXS) measurements (Figure S5, Supporting Information), which provide more surface-sensitive structural insights. These results also show negligible differences in crystalline orientation or texture between annealed and unannealed PTAA cases, reinforcing the view that film crystallinity is not significantly influenced by HTL wetting behavior under our processing conditions. This conclusion is consistent with prior literature, including the recent study by Tan et al.,[28] which reports that wetting layer modification—while it is critical for controlling nucleation uniformity and interfacial contact—does not always lead to measurable changes in perovskite crystallinity in XRD or GIWAXS data, especially when grain growth is kinetically controlled. In terms of morphology, scanning electron microscopy (SEM) images (Figure S6, Supporting Information) reveal that the surface morphology of the perovskite is dense and shows no noticeable differences for the perovskite layer made on varied HTL. However, cross-sectional SEM images indicate that the perovskite prepared on the annealed HTL exhibits significant voids. Then, we investigated the bottom interface of the perovskite layer for PTAA and PTAA-A (Figure S7, Supporting Information). The findings demonstrate that non-annealed PTAA generates a comparatively homogenous bottom interface in the absence of voids. In

J.-W. Chiou
Department of Applied Physics
National University of Kaohsiung
Room 522, Science Building, No.700, Gaoxiongdaxue Rd. Nanzi Dist., Kaohsiung City 81148, Taiwan
J.-M. Lin
National Synchrotron Radiation Research Center
101 Hsin-Ann Road, Hsinchu Science Park, Hsinchu 300092, Taiwan

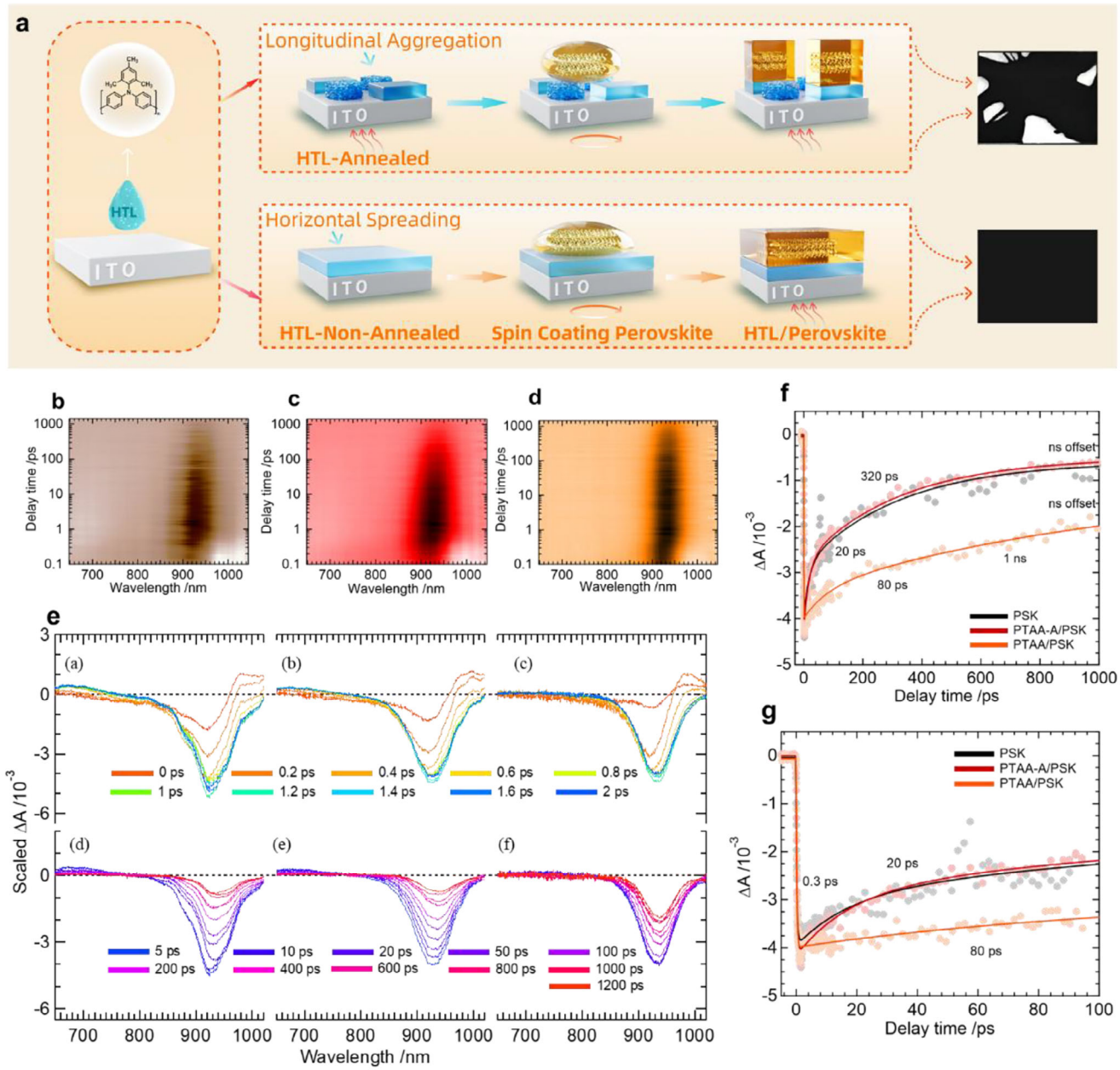

Figure 1. The fabrication of hole-transporting layers and performance of tin-lead perovskite solar cells. a) The schematic of HTL fabrication with and without annealing. Femtosecond transient absorption spectrograms of the Sn-Pb perovskite films for (b) pristine perovskite, c) annealed PTAA/perovskite, and d) unannealed PTAA/perovskite. e) Femtosecond transient absorption spectra of Sn-Pb perovskite films for pristine perovskite (left), annealed PTAA/perovskite (middle), and unannealed PTAA/perovskite (right). Femtosecond transient kinetics of Sn-Pb perovskite films monitored at the PB band minima at (f) long delay times and g) short delay times.

contrast, annealed PTAA shows hydrophobic particles formed by the aggregated HTL, which inhibit nucleation and growth of the perovskite in those areas.

Considering the film coverage, we did not prepare annealed films with low coverage using Spiro-A, TAPC-A, and m-MTDATA-A as HTLs. Instead, we compared TLPSC devices fabricated on PTAA and PTAA-A HTLs. The results (Figure S8, Supporting Information) show that the PCE of the cell with annealed PTAA is only 18.72%, with an open circuit voltage (V_{OC}) of 0.81 V, a current–density (J_{SC}) of 30.59 mA cm^{-2}, and a fill factor (FF) of 75.51%. In contrast, the non-annealed PTAA-based cell achieved a higher PCE of 22.67%, with a V_{OC} of 0.86 V, a J_{SC} of 33.00 mA cm^{-2}, and an FF of 86%. This improvement is attributed to the insufficient coverage of PTAA after longitudinal aggregation during annealing, as further confirmed by AFM-IR imaging measurements (Figure S9, Supporting Information).

The efficiencies of non-annealed Spiro, TAPC, and m-MTDATA HTLs are lower than that of PTAA (Figure S10,

Supporting Information). However, their highest efficiencies still exceed 20%, demonstrating that the non-annealing method offers a certain degree of general applicability. PTAA achieves better performance because it is a polymer semiconductor with strong hole transport capabilities. Among them, the lower efficiency of Spiro-based cells may be attributed to their relatively shallow valence band position measured by the UPS technique (Figure S11, Supporting Information).

The femtosecond transient absorption spectrograms (TAS) and selected spectral traces of pristine Sn-Pb perovskite and the perovskite films grown on annealed and unannealed polymeric PTAA HTLs (Figure 1b–e) show signals due to photobleaching (PB) of the band edge states at ≈920 nm and photoinduced absorption (PIA) due to hot carriers on the longer wavelength side of the PB band. The PB band shows a slight red shift when grown on PTAA underlayers, probably due to band bending at the interface between the PTAA and perovskite. Both the spectrogram and the transient spectral traces show that PB bands are longer lived in the case of perovskite films grown on unannealed PTAA underlayers. The longer lifetimes of the perovskite films in the presence of hole-transporting underlayers reflect retarded charge recombination due to effective charge separation at the interface between PTAA and perovskite.[29] Further, transient kinetics were monitored at the PB band minima of the recorded samples (Figure 1f,g; Table S2, Supporting Information). Both pristine and film grown on annealed PTAA reflect similar decay behaviors, whereas the film grown on unannealed PTAA shows retarded kinetics with the 20 ps (PTAA-A) decaying component retarded to 80 ps (PTAA) and the 320 ps (PTAA-A) retarded to 1 ns (PTAA). The picosecond decaying components were attributed to some non-radiative trap-mediated decay processes as described elsewhere.[30,31] The TAS results thus conformed that the perovskite layer deposited on the non-annealing PTAA substrate exhibited much slower charge recombination compared to that on the PTAA-A film.

To further corroborate the carrier dynamics observed in TAS, we conducted steady-state and time-resolved photoluminescence (PL and TRPL) measurements on Sn–Pb perovskite films deposited atop different HTLs. The PL spectra (Figure S12, Supporting Information) show pronounced quenching for the perovskite grown on unannealed PTAA, indicating more efficient interfacial hole extraction due to stronger electronic coupling at the HTL/perovskite interface. This quenching results from rapid charge transfer from the photoexcited perovskite to the HTL, thus reducing radiative recombination. Complementarily, the TRPL decay profiles (Figure S13, Supporting Information) reinforce this conclusion by showing a substantial decrease in carrier lifetime with unannealed PTAA. Specifically, the lifetime (τ) drops from 372.6 ns for pristine perovskite to 223.4 ns for annealed PTAA and further to 110.2 ns for unannealed PTAA. This consistent shortening of τ with increased hole extraction ability aligns well with the PL results, and confirms the improved charge separation at the unannealed PTAA/perovskite interface. Taken together, these photoluminescence analyses visually and quantitatively support the interpretation of enhanced interfacial hole extraction for the unannealed PTAA substrate, in excellent agreement with the TAS results.

To complement this morphological observation and verify the interfacial role of the SnF_2 additive, we further conducted TOF-SIMS depth profiling, targeting fluorine (F^-) as the characteristic ion of SnF_2. As shown in Figure S14 (Supporting Information), the unannealed PTAA sample exhibits a significantly stronger and sharper F^- signal near the buried HTL/perovskite interface. These results confirm that SnF_2 preferentially accumulates near the interface in unannealed films. The thermal treatment of PTAA appears to hinder such interfacial retention by densifying the polymer matrix. To thoroughly examine the effects of different PTAA treatments on the perovskite bottom interface, we conducted a detailed study by washing the perovskite films with N,N-dimethylformamide (DMF) to evaluate the retention of critical components (**Figure 2**a). Regardless of whether the PTAA layer was annealed or not, the PbI_2 signal remained weak after two washes, indicating that the bulk perovskite material did not interact with PTAA. However, the persistence of SnF_2 was markedly stronger in the unannealed PTAA films compared to the annealed ones, suggesting a more robust interaction between SnF_2 and unannealed PTAA. This stronger binding in the unannealed PTAA likely arises from better dispersion of SnF_2 in the polymer matrix, enabling stable interactions that resist dissolution during the DMF washing process. In contrast, in annealed PTAA, the aggregation of polymer chains limits the incorporation and retention of SnF_2, weakening its interaction.

We performed synchrotron-based XPS measurements with an excitation energy of 750 eV to enhance surface and interface sensitivity. The C 1s spectrum (Figure S15, Supporting Information) of the unannealed PTAA sample clearly reveals a distinct C–F component with an integrated contribution of ≈3.2%, indicating the presence of fluorine-containing species such as SnF_2 at or near the buried interface. To gain further insights into the structural changes induced by SnF_2, we employed synchrotron small-angle X-ray scattering (SAXS) to analyze the dispersion states of PTAA and PTAA/SnF_2 solutions and to elucidate the role of SnF_2 in modifying the polymer's microstructure (Figure 2b,c).[32–35] The SAXS data were quantitatively analyzed (Table S2, Supporting Information) using the Beaucage unified equation,[36,37] which revealed three distinct structural levels of aggregation. At the largest scale (level 1), compact aggregates were characterized by a power-law exponent near 4, signifying dense particle-like structures for both samples. The size of these aggregates (radius of gyration, Rg) was ≈48 nm for both PTAA and PTAA/SnF_2, indicating that the aggregate size remained consistent across the samples. The intermediate scale (level 2) was represented by fractal network aggregates with a mass fractal dimension of ≈2.2 for the PTAA only sample, indicative of loosely connected structures (top in Figure 2d). In PTAA/SnF_2 solutions, the fractal dimension increased to 2.8, reflecting the formation of tighter and more interconnected networks due to SnF_2 crosslinking (bottom in Figure 2d). The Rg for these networks also increased from ≈7.5 nm in PTAA to ≈9.4 nm in PTAA/SnF_2, further supporting the idea of structural densification. The smallest scale (level 3), the rod-like polymer segments exhibited similar scattering behavior across both PTAA and PTAA/SnF_2, with $Iq{\sim}q^{-1}$, indicating that the fundamental polymer structure was retained regardless of SnF_2 addition. The results confirm that SnF_2 significantly enhances the structural organization of PTAA, creating denser and more interconnected networks. This improved aggregation is attributed to a combination of π–π interactions and SnF_2-induced crosslinking, which enhances the

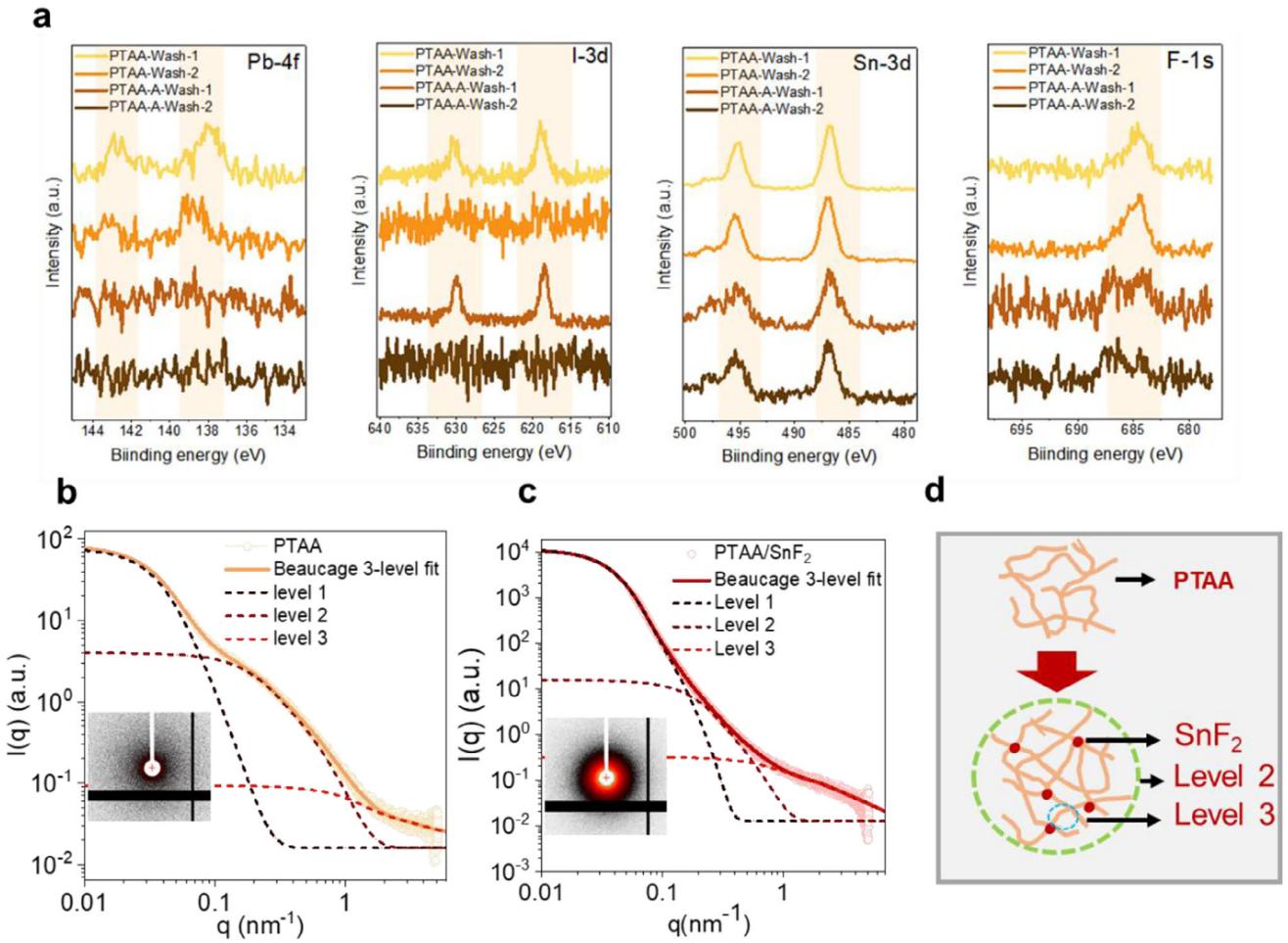

Figure 2. Characterization of the Interaction between PTAA and SnF_2. a) XPS spectra of Pb-I-Sn-F for PTAA-annealed and unannealed perovskite films washed with DMF once and twice. All films were all fabricated on quartz glass. b) Fitting results for the SAXS profile of the PTAA solution using the Beaucage unified equation with three structural levels. The solid curve represents the overall fit, while the dashed curves correspond to the scattering contributions from each level. c) Fitting results for the SAXS profile of the PTAA/SnF_2 solution using the Beaucage unified equation with three structural levels. The solid curve represents the overall fit, while the dashed curves correspond to the scattering contributions from each level. d) Schematic illustrations of the aggregation of PTAA and PTAA/SnF_2.

retention of SnF_2 in unannealed films and promotes a uniform interface with the perovskite layer. These structural enhancements are critical for improving interfacial properties, reducing defect density, and enhancing the charge transport property in perovskite solar cells.

We also analyzed the SAXS spectra of PEDOT:PSS and other HTLs with and without the addition of SnF_2 (Figure S16, Supporting Information). The scattering profiles for PEDOT:PSS and PEDOT:PSS + SnF_2 do not show significant changes. This suggests that SnF_2 has minimal interaction with PEDOT:PSS. The negligible aggregation indicates that the structure and properties of PEDOT:PSS remain largely unchanged after the addition of SnF_2. In TAPC, Spiro, and m-MTDATA, SnF_2 induces significant aggregation, mirroring the behavior observed in PTAA. This supports the hypothesis that SnF_2 interacts with nitrogen-containing systems to form compact aggregates and improve structural integrity. The increased aggregation in the mid-q (level 2) region for all these materials suggests that SnF_2 facilitates crosslinking and densification, improving the interface between the HTL and the perovskite layer. The aggregation induced by SnF_2 improves the network density of TAPC, Spiro, and m-MTDATA, potentially enhancing the stability and charge transport properties of these HTLs. The similar aggregation behavior observed in PTAA, TAPC, Spiro, and m-MTDATA highlights the universality of SnF_2 as a structural modifier for HTLs except for PEDOT:PSS. The findings suggest that SnF_2 can be used to tailor the properties of nitrogen-containing HTLs, offering a pathway to optimize interfacial properties for improved device performance.

We performed Grazing Incidence Small-Angle X-ray Scattering (GISAXS) measurements for the annealed and non-annealed PTAA thin-film samples (Figure S17, Supporting Information). The scattering intensity of the non-annealed PTAA is higher than that of the annealed PTAA in the low-q region ($q < 0.1$ nm^{-1}). This indicates the presence of larger-scale structures in the non-annealed sample. Annealing induces longitudinal aggregation of PTAA molecules through π–π stacking, which disrupts the uniformity of the polymer network and reduces larger-scale aggregation. This effect is visible in the lower intensity in the low-q

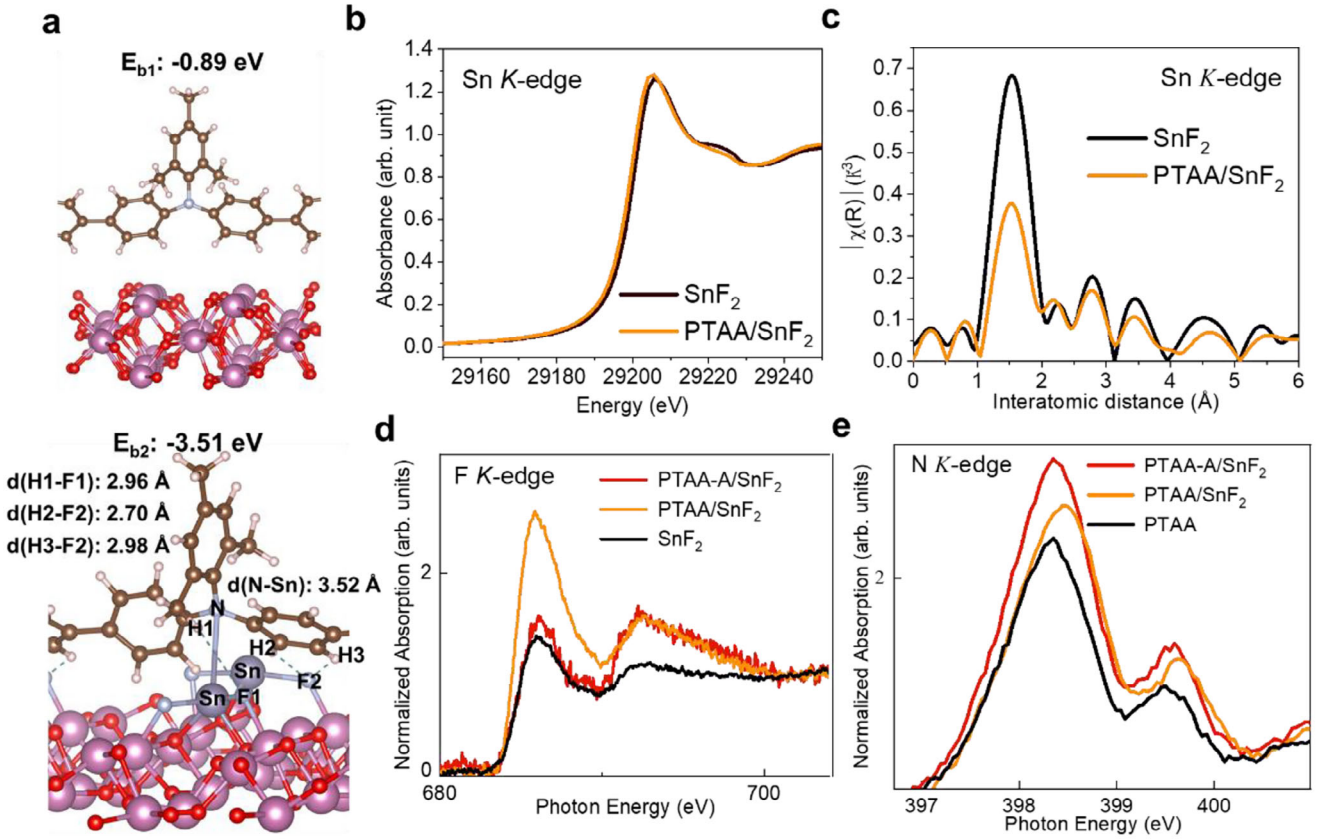

Figure 3. Interaction analysis between PTAA and SnF_2. a) DFT-optimized structures of without (top) and with (bottom) SnF_2 adsorbed on the PTAA-In_2O_3 surface, with representative interactions labeled. b) XANES and c) EXAFS of Sn K-edge in PTAA and PTAA with SnF_2 solution. Soft-X-ray absorption of (d) F K-edge and e) N K-edge for PTAA-A and PTAA with SnF_2.

region, indicating fewer large aggregates in the annealed PTAA sample. The higher scattering intensity suggests that the absence of annealing preserves the uniform polymer structure, avoiding the formation of dense, localized aggregates. This uniformity is beneficial for creating smoother interfaces and enhancing film coverage, as observed in other characterizations like AFM and SEM. Non-annealed PTAA provides a smoother and more consistent interface with the perovskite layer, improving wettability and reducing void formation, leading to enhanced charge transport and reduced current leakage.

The results from the adsorption model DFT calculations (**Figure** 3a) indicate that the N-Sn distance (3.52 Å) is significantly smaller than the sum of the van der Waals radii of Sn and F, which is 4.08 Å, suggesting the formation of a non-covalent interaction (dangling bond) between N and SnF_2. The sum of the van der Waals radii for F and H is 2.66 Å, implying that among all F-H interactions, F2-H2 can be considered as a noticeable hydrogen bond (Table S5, Supporting Information). To verify the stability of SnF_2 adsorption on the PTAA-covered In_2O_3 surface, the binding energy of PTAA on the In_2O_3 surface (E_{b1}: −0.89 eV) was compared with the binding energy of SnF_2 adsorbed on PTAA-anchored In_2O_3 (E_{b2}: −3.51 eV). The more negative E_{b2} indicates that SnF_2 tends to bind simultaneously with PTAA and In_2O_3, thereby reducing the system's energy.

To investigate the PTAA assembly induced by SnF_2, we conducted a series of X-ray absorption spectroscopy (XAS) measurements. First, we examined the Sn K-edge X-ray absorption near-edge structure (XANES, Figure 3b), in which the introduction of SnF_2 in PTAA shifted the absorption edge to lower energy and thus decreased the average oxidation number of Sn. It was attributed to the tin-fluorine de-coordination, unveiled by extended X-ray absorption fine structure (EXAFS, Figure 3c). The intensity of the tin-fluorine path (interatomic distance of 1.54 Å) decreased to half intensity upon introducing PTAA because N and Sn would form a dangling bond between PTAA and SnF_2 for tin to reduce its oxidation number. Moreover, we also inspected the F K-edge XANES (Figure 3d), showing that the rising absorption edge (white line) of non-annealed PTAA-SnF_2 is higher than that of annealed PTAA-SnF_2 and pristine SnF_2 to give a higher average valence number for the former than for the latter. It supported our argument that PTAA induces tin-fluorine de-coordination. Then, we also measured the N K-edge XANES to evaluate the function of PTAA with and without annealing. The white line of annealed PTAA-SnF_2 was higher than pure PTAA (Figure 3e), indicating a higher average valence number in the presence of SnF_2. It indicates that the lone pair of the N on PTAA chelates with the Sn ions, with less coordination to donate electrons to the Sn ions. The lower electron negativity of the N ions than the F ions also resulted in the decreased average oxidation number of Sn. For

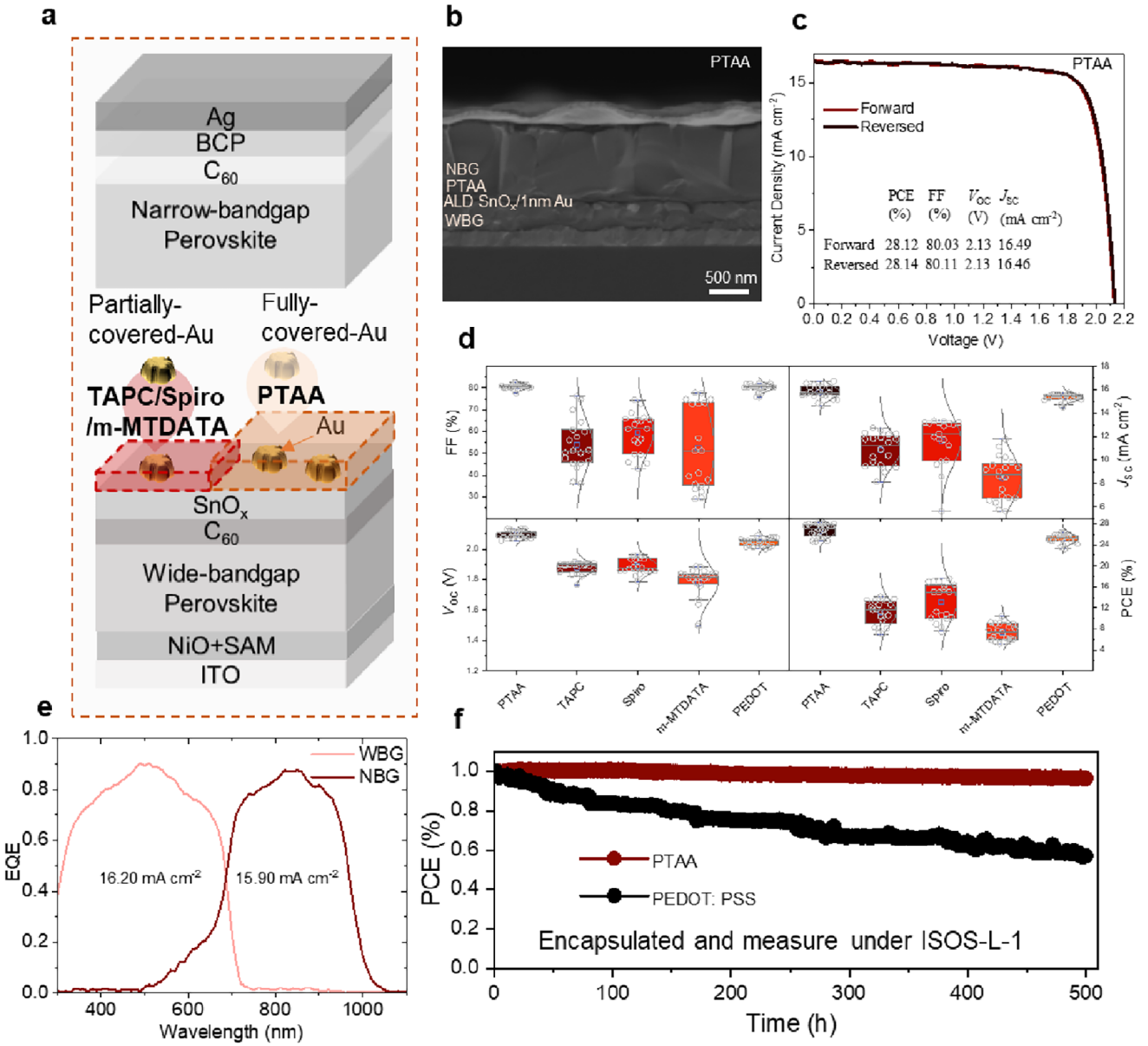

Figure 4. Device performance and stability. a) Device architecture; b) Cross-sectional SEM image of tandem; c) J–V curves of the PTAA-based all-perovskite tandem solar cells; d) PCE statistic of PTAA, TAPC, Spiro, m-MTDATA, and PEDOT:PSS tandem cells; e) EQE of PTAA tandem cells measured under reverse and forward scans; f) MPP stability tracking of PTAA and PEDOT:PSS tandem devices under simulated one-sun illumination at 50% relative humidity (RH).

the non-annealed PTAA-SnF_2 sample, the white line shifted to a higher energy region, indicating the strong interaction between N and Sn. It is consistent with the DFT results showing the formation of a dangling bond between N and Sn. Thus, the interaction between the less-coordinated Sn ions in PTAA induced the PTAA assembling, leading to superior interfacial charge transport and excellent photovoltaic behaviors.

We independently produced PTAA and PTAA-SnF_2 solutions on lace mesh grids and performed transmission electron microscope (TEM) investigation (Figure S18, Supporting Information). The dark spots in the TEM pictures signify places of considerable aggregation. Following the introduction of SnF_2, PTAA demonstrated an increased level of aggregation. Energy-dispersive X-ray spectroscopy (EDS) verified that SnF_2 is homogeneously distributed inside the PTAA matrix, signifying its significant involvement in promoting PTAA aggregation (Figure S19, Supporting Information).

We carried out Electron Paramagnetic Resonance (EPR) spectral measurements (Figure S20, Supporting Information) to compare the charge-separation property for PTAA, SnF_2, and their mixture (both under normal conditions and after 18 min of solar light exposure). When PTAA is mixed with SnF_2, the EPR signal at g-factor ≈2.00 increases slightly in intensity compared to pure PTAA. This suggests that SnF_2 induces additional

unpaired electronic states in PTAA through charge transfer or interaction between Sn and the PTAA. Upon solar light exposure, the EPR signal intensity increases significantly compared to the mix without light exposure. This indicates enhanced generation of unpaired electrons, which could arise from light-induced charge separation facilitated by the interaction between PTAA and SnF_2. The significant increase in the EPR signal after 18 min of solar light exposure indicates that the PTAA-SnF_2 mixture exhibits photoactive behavior. This could result from light-induced charge transfer at the PTAA/SnF_2 interface, where SnF_2 may act as an electronic modifier, enhancing the separation of photo-generated charges. The increased unpaired electrons imply that the interaction creates longer-lived charge-separated states, which are crucial for improving charge transport and reducing recombination in photovoltaic applications. These findings highlight the role of SnF_2 in improving the performance of PTAA-based hole transport layers, supporting its use in advanced perovskite solar cell designs. Un-annealing PTAA is the key to the strong interaction between SnF_2 and PTAA that eventually enhances the device performance observed herein.

We fabricated tandem solar cells (**Figure** 4a–d) for the champion device to achieve 28.14 (28.12)% with a V_{OC} of 2.13 (2.13) V, a J_{SC} of 16.46 (16.49) mA cm^{-2} and a FF of 80.11 (80.03)% under reverse (forward) scans (Figure 4c). Using HTLs such as TAPC, Spiro, and m-MTDATA leads to poor coverage of the perovskite (Figure 4a), resulting in incomplete gold contact and increased leakage paths that give poorer performance than the PTAA (Figure 4d). PTAA, as the HTL, ensures full coverage, mitigating leakage issues and improving charge collection efficiency. The presence of SnF_2 in PTAA further enhances interfacial charge transport through crosslinking and improved polymer aggregation, reducing recombination losses. The cross-sectional SEM image (Figure 4b) shows the device structure of the all-perovskite tandem solar cells, with a well-defined interface between the narrow-bandgap perovskite (NBG), PTAA, wide-bandgap perovskite (WBG), and the NiOx/SAM layers. This uniformity ensures better charge transport and reduces defect-induced recombination. Figure 4e shows the EQE spectra of the champion tandem perovskite solar cell. Both sub-cells exhibit high EQE values over 80% and closely match the photocurrents of 16.20 mA cm^{-2} (WBG) and 15.90 mA cm^{-2} (NBG). This current matching ensures efficient tandem operation, while the broad spectral response highlights the device's ability to leverage complementary absorption, supporting its high-power conversion efficiency. According to statistical data (Figure 4d), the *Voc* values of the PTAA devices exceed 2 V, while the *Voc* of the three small molecules, TAPC, Spiro, and m-MTDATA, remain below 2 V. This indicates that PTAA molecules exhibit lower current leakage, whereas the insufficient coverage of small molecules may result in direct contact between gold and the perovskite, leading to current leakage. We tested the stability using maximum power point (MPP) tracking in air and under simulated one-sun illumination (Figure 4f). We found that encapsulated PTAA-based tandem solar cells can prove above 500 h stability under ISOS-L-1, significantly outperforming PEDOT:PSS-based devices, which show a T_{90} of only 40 h under the same ambient air conditions. This is the first example of all-perovskite tandem solar cells fabricated with hydrophobic PTAA as HTL for the NBG to attain device performance over 28%.

3. Conclusion

This study presents a universal non-annealing method for fabricating hole transport layers in tin-lead mixed and tandem perovskite solar cells, overcoming key limitations of traditional annealing processes. By incorporating SnF_2 without annealing, the uniform polymeric network of PTAA was formed, promoting tighter aggregation and improved interfacial properties. Synchrotron SAXS, GISAXS, and TEM analyses reveal that SnF_2-induced crosslinking creates compact polymer structures with increased fractal dimensions, enabling the formation of defect-free perovskite films. Synchrotron XAS (XANES and EXAFS), EPR, XPS, and DFT studies demonstrate that SnF_2 forms a dangling bond with the N atom of PTAA, and this facilitates charge transfer, leading to long-lived charge-separated states critical for reducing charge recombination losses, confirmed by the femtosecond TAS measurements. The non-annealed PTAA-based devices achieve a power conversion efficiency of 22.67%, outperforming the annealed counterparts with PCE 18.72%. When extended to tandem solar cells, the method achieves a record PCE of 28.14%, with excellent current matching and stability, retaining 96% of the initial efficiency after 500 h of illumination under operational conditions. The universality of this approach is confirmed by its successful applications to other HTLs, such as Spiro, TAPC, and m-MTDATA, with efficiencies exceeding 20% as NBG TLPSCs. These results highlight the scientific advancements enabled by SnF_2, which acts as both a chemical crosslinker and structural/electronic modifier. This work provides critical insights into HTL design, paving the way for high-efficiency and stable perovskite solar cells, and advancing their potential for future commercialization.

Supporting Information

Supporting Information is available from the Wiley Online Library or from the author.

Acknowledgements

The authors gratefully acknowledge the support by the National Science and Technology Council (NSTC), Taiwan (Grant Nos. NSTC 113-2639-M-A49-001-ASP and NSTC 114-2639-M-A49-001-ASP), and the Center for Emergent Functional Matter Science of National Yang-Ming Chiao-Tung University (NYCU) from the Featured Areas Research Center Program within the framework of the Higher Education Sprout Project by the Ministry of Education (MOE) in Taiwan. The authors thank E. Jokar and Y.-J. Xue for valuable discussions. The authors also sincerely thank C.-H. Kuo, Y.-H. Chang, P. Rajamanickam, for their support of the experiments. The authors gratefully thank Ms. C.-Y. Chien of NTU Instrumentation Center for the assistance in FE-TEM and EDS experiments. The authors also thank Ms. J.-C. Chen of the NTHU Instrumentation Center for assistance in the EPR measurements. The authors gratefully thank the National Synchrotron Radiation Research Center (NSRRC), Taiwan, for the XAS (hard X-ray TLS 01C1 beamlines and soft X-ray TPS 45A2 beamline) and SAXS (TPS 25A1 beamline) measurements. The authors thank Dr. Y.-W. Tsai and Dr. J.-M. Lin (TPS 25A1, NSRRC) for their kind assistance in GIWAXS data analysis. The authors also thank Dr. B.-H. Liu and Dr. C-H. Wang (TLS 24A1, NSRRC) for their kind assistance in C XPS data analysis.

Conflict of Interest

The authors declare no conflict of interest.

Author Contributions

C.-H.K., X.J., and Q.Z. contributed equally to this work. E.W.-G.D. and Y.H. conceived the project and designed the experiments. C.-H.K. fabricated the devices and was involved in all the experimental parts. C.-H.K., X.J., and Q.Z. contributed to characterizations and data analysis. X.W. performed the DFT calculation and analysis. S.-F.H. performed the EXAFS and XANES analysis. J.-M.L. performed the SAXS measurements. H.-L.C. performed the SAXS analysis. Y.-S.S. supported the device fabrication and characterizations. S.N. performed the TAS measurements and analysis. J.-W.C. performed the soft X-ray measurements and analysis. C.-H.K. and X.J. drafted the manuscript. E.W.-G.D. completed the final manuscript.

Data Availability Statement

Research data are not shared.

Keywords

all perovskite tandem solar cell, hydrophobicity, non-annealing, PTAA, tin-lead perovskite solar cell

Received: August 25, 2025
Revised: September 9, 2025
Published online:

[1] S. Zhou, S. Fu, C. Wang, W. Meng, J. Zhou, Y. Zou, Q. Lin, L. Huang, W. Zhang, G. Zeng, D. Pu, H. Guan, C. Wang, K. Dong, H. Cui, S. Wang, T. Wang, G. Fang, W. Ke, *Nature* **2023**, *624*, 69.
[2] Z. Liu, R. Lin, M. Wei, M. Yin, P. Wu, M. Li, L. Li, Y. Wang, G. Chen, V. Carnevali, L. Agosta, V. Slama, N. Lempesis, Z. Wang, Y. Deng, H. Luo, H. Gao, U. Rothlisberger, S. M. Zakeeruddin, X. Luo, Y. Liu, M. Grätzel, H. Tan, *Nat. Mater.* **2025**, *24*, 252.
[3] F. Yang, K. Zhu, *Adv. Mater.* **2024**, *36*, 2314341.
[4] J. Tong, Q. Jiang, A. J. Ferguson, A. F. Palmstrom, X. Wang, J. Hao, S. P. Dunfield, A. E. Louks, S. P. Harvey, C. Li, *Nat. Energy* **2022**, *7*, 642.
[5] J. Lim, N.-G. Park, S. I. Seok, M. Saliba, *Energy Environ. Sci.* **2024**, *17*, 4390.
[6] Z. Li, B. Li, X. Wu, S. A. Sheppard, S. Zhang, D. Gao, N. J. Long, Z. Zhu, *Science* **2022**, *376*, 416.
[7] C. Liu, Y. Yang, H. Chen, I. Spanopoulos, A. S. Bati, I. W. Gilley, J. Chen, A. Maxwell, B. Vishal, R. P. Reynolds, *Nature* **2024**, *633*, 359.
[8] S. Fu, S. Zhou, W. Meng, G. Li, K. Dong, D. Pu, J. Zhou, C. Wang, H. Guan, W. Shao, L. Huang, Z. Su, C. Wang, G. Chen, P. Jia, J. Wang, Z. Xu, X. Gao, H. Cong, T. Wang, C. Xiao, G. Fang, W. Ke, *Nat. Nanotechnol.* **2025**, *20*, 764.
[9] Y. Wang, R. Lin, C. Liu, X. Wang, C. Chosy, Y. Haruta, A. D. Bui, M. Li, H. Sun, X. Zheng, H. Luo, P. Wu, H. Gao, W. Sun, Y. Nie, H. Zhu, K. Zhou, H. T. Nguyen, X. Luo, L. Li, C. Xiao, M. I. Saidaminov, S. D. Stranks, L. Zhang, H. Tan, *Nature* **2024**, *635*, 867.
[10] J. Wang, L. Zeng, D. Zhang, A. Maxwell, H. Chen, K. Datta, A. Caiazzo, W. H. Remmerswaal, N. R. Schipper, Z. Chen, *Nat. Energy* **2024**, *9*, 70.
[11] S. Liu, Y. Lu, C. Yu, J. Li, R. Luo, R. Guo, H. Liang, X. Jia, X. Guo, Y.-D. Wang, *Nature* **2024**, *628*, 306.
[12] S. Hu, J. Wang, P. Zhao, J. Pascual, J. Wang, F. Rombach, A. Dasgupta, W. Liu, M. A. Truong, H. Zhu, M. Kober-Czerny, J. A. Drysdale, J. A. Smith, Z. Yuan, G. J. W. Aalbers, N. R. M. Schipper, J. Yao, K. Nakano, S.-H. Turren-Cruz, A. Dallmann, M. G. Christoforo, J. M. Ball, D. P. McMeekin, K.-A. Zaininger, Z. Liu, N. K. Noel, K. Tajima, W. Chen, M. Ehara, R. A. J. Janssen, et al., *Nature* **2025**, *639*, 93.
[13] Y. Yang, H. Chen, C. Liu, J. Xu, C. Huang, C. D. Malliakas, H. Wan, A. S. Bati, Z. Wang, R. P. Reynolds, *Science* **2024**, *386*, 898.
[14] Y. Yang, C. Liu, Y. Ding, B. Ding, J. Xu, A. Liu, J. Yu, L. Grater, H. Zhu, S. S. Hadke, *Nat. Energy* **2024**, *9*, 316.
[15] F. Jiang, Y. Shi, T. R. Rana, D. Morales, I. E. Gould, D. P. McCarthy, J. A. Smith, M. G. Christoforo, M. Y. Yaman, F. Mandani, *Nat. Energy* **2024**, *9*, 1275.
[16] X. Liao, X. Jia, W. Li, X. Lang, J. Zhang, X. Zhao, Y. Ji, Q. Du, C.-H. Kuan, Z. Ren, W. Huang, Y. Bai, K. Zhang, C. Xiao, Q. Lin, Y.-B. Chen, J. Tong, *Nat. Commun.* **2025**, *16*, 1164.
[17] M. Li, J. Yan, A. Zhang, X. Zhao, X. Yang, S. Yan, N. Ma, T. Ma, D. Luo, Z. Chen, L. Li, X. Li, C. Chen, H. Song, J. Tang, *Joule* **2025**, *9*, 101825.
[18] S. Fu, N. Sun, Y. Xian, L. Chen, Y. Li, C. Li, A. Abudulimu, P. N. Kaluarachchi, Z. Huang, X. Wang, K. Dolia, D. S. Ginger, M. J. Hehen, R. J. Ellingson, B. Chen, E. H. Sargent, Z. Song, Y. Yan, *Joule* **2024**, *8*, 2220.
[19] J. Zhu, Y. Xu, Y. Luo, J. Luo, R. He, C. Wang, Y. Wang, K. Wei, Z. Yi, Z. Gao, J. Wang, J. You, Z. Zhang, H. Lai, S. Ren, X. Liu, C. Xiao, C. Chen, J. Zhang, F. Fu, D. Zhao, *Sci. Adv.* **2024**, *10*, adl2063.
[20] Q. Jiang, K. Zhu, *Nat. Rev. Mater.* **2024**, *9*, 399.
[21] K. Xiao, Y.-H. Lin, M. Zhang, R. D. Oliver, X. Wang, Z. Liu, X. Luo, J. Li, D. Lai, H. Luo, *Science* **2022**, *376*, 762.
[22] C. Li, Y. Chen, Z. Zhang, C. Liu, F. Guo, W. Ahmad, P. Gao, *Energy Environ. Sci.* **2024**, *17*, 6157.
[23] J. Zeng, Z. Liu, D. Wang, J. Wu, P. Zhu, Y. Bao, X. Guo, G. Qu, B. Hu, X. Wang, *J. Am. Chem. Soc.* **2024**, *147*, 725.
[24] Y. Wang, L. Duan, M. Zhang, Z. Hameiri, X. Liu, Y. Bai, X. Hao, *Sol. RRL* **2022**, *6*, 2200234.
[25] C. Fei, N. Li, M. Wang, X. Wang, H. Gu, B. Chen, Z. Zhang, Z. Ni, H. Jiao, W. Xu, Z. Shi, Y. Yan, J. Huang, *Science* **2023**, *380*, 823.
[26] J. Chen, J. Du, J. Cai, B. Ouyang, Z. Li, X. Wu, C. Tian, A. Sun, R. Zhuang, X. Wu, J. Cai, Y. Zhao, R. Li, T. Xue, T. Cen, K. Zhao, C.-C. Chen, *ACS Energy Lett.* **2025**, *10*, 1117.
[27] J. Kurisinkal Pious, Y. Zwirner, H. Lai, S. Olthof, Q. Jeangros, E. Gilshtein, R. K. Kothandaraman, K. Artuk, P. Wechsler, C. Chen, C. M. Wolff, D. Zhao, A. N. Tiwari, F. Fu, *ACS Appl. Mater. Interfaces* **2023**, *15*, 10150.
[28] S. Zhang, F. Ye, X. Wang, R. Chen, H. Zhang, L. Zhan, X. Jiang, Y. Li, X. Ji, S. Liu, M. Yu, F. Yu, Y. Zhang, R. Wu, Z. Liu, Z. Ning, D. Neher, L. Han, Y. Lin, H. Tian, W. Chen, M. Stolterfoht, L. Zhang, W.-H. Zhu, Y. Wu, *Science* **2023**, *380*, 404.
[29] D. Song, S. Narra, M.-Y. Li, J.-S. Lin, E. W.-G. Diau, *ACS Energy Lett.* **2021**, *6*, 4179.
[30] S. Narra, E. Jokar, O. Pearce, C.-Y. Lin, A. Fathi, E. W.-G. Diau, *J. Phys. Chem. Lett.* **2020**, *11*, 5699.
[31] S. Narra, C.-Y. Lin, A. Seetharaman, E. Jokar, E. W.-G. Diau, *J. Phys. Chem. Lett.* **2021**, *12*, 12292.
[32] W.-C. Ou-Yang, C.-S. Chang, H.-L. Chen, C.-S. Tsao, K.-Y. Peng, S.-A. Chen, C. C. Han, *Phys. Rev. E* **2005**, *72*, 031802.
[33] Y.-C. Li, K.-B. Chen, H.-L. Chen, C.-S. Hsu, C.-S. Tsao, J.-H. Chen, S.-A. Chen, *Langmuir* **2006**, *22*, 11009.
[34] M. H. Rahman, C.-Y. Chen, S.-C. Liao, H.-L. Chen, C.-S. Tsao, J.-H. Chen, J.-L. Liao, V. A. Ivanov, S.-A. Chen, *Macromolecules* **2007**, *40*, 6572.
[35] M. Knaapila, V. Garamus, F. Dias, L. Almásy, F. Galbrecht, A. Charas, J. Morgado, H. Burrows, U. Scherf, A. Monkman, *Macromolecules* **2006**, *39*, 6505.
[36] G. Beaucage, *J. Appl. Crystallogr.* **1995**, *28*, 717.
[37] G. Beaucage, *J. Appl. Crystallogr.* **1996**, *29*, 134.